FIRST-PRINCIPLE INVESTIGATION OF La$_{0.7}$Ba$_{0.3}$Mn$_{(1-x)}$Fe$_x$O$_3$ STRUCTURAL PROPERTIES USING CASTEP

Sitti Ahmiatri Saptari*[1], Sarah Aulia[1], Ryan Rizaldy[1], and Anugrah Azhar[2]

[1] Department of Physics, UIN Syarif Hidayatullah, Jakarta, Indonesia
[2] Department of Physics and Astronomy, The University of Manchester, Oxford Road,
Manchester, United Kingdom
*sitti.ahmiatri@uinjkt.ac.id

ABSTRACT

We conducted first-principles Density Functional Theory (DFT) calculations using the CASTEP software package to investigate the crystal structure and mechanical properties of Fe^{3+}-doped La$_{0.7}$Ba$_{0.3}$MnO$_3$ material at the Mn^{3+} site, with doping concentrations ranging up to 50%. Through geometry optimization, we simulated the X-ray diffraction (XRD) pattern. We observed that the doping of Fe did not result in a shift in the peak positions of the diffraction pattern. However, it led to an increase in intensity at the [012] peak and the splitting of peaks [104] and [110]. Regarding the mechanical properties, we examined the elastic constants and observed a reduction in the Bulk, Shear, and Young's modulus values. The Shear and Bulk modulus and Poisson's ratio indicated that La$_{0.7}$Ba$_{0.3}$Mn$_{(1-x)}$Fe$_x$O$_3$ becomes less ductile with increased Fe^{3+} doping content. Furthermore, we performed calculations for the Debye temperature, which revealed a decrease in the thermal conductivity of the La$_{0.7}$Ba$_{0.3}$Mn$_{(1-x)}$Fe$_x$O$_3$ material.

Keywords: DFT; La$_{0.7}$Ba$_{0.3}$Mn$_{(1-x)}$Fe$_x$O$_3$; CASTEP; XRD simulation; elastic constant

INTRODUCTION

Perovskite manganite is a versatile material with a wide range of properties, including structural, magnetic, electrical, and absorber properties, that can be deliberately engineered and manipulated[1]. Perovskite materials are characterized by the chemical formula ABO$_3$. In the case of manganate perovskite materials, they are extensively engineered using the formula A$_{(1-x)}$B$_x$MnO$_3$. The A element represents a trivalent rare earth element, while the B denotes a bivalent alkaline earth metal[2–4]. This deliberate engineering profoundly influences the crystal structure and the resulting magnetization value of the material. Recent research in doping Lanthanum-based perovskites [5–8] strengthens the argument that explained doping on the La site of lanthanum manganate material induces the presence of two valence states for Mn ions, namely Mn^{3+} and Mn^{4+}, due to double exchange interaction events. Furthermore, doping on the Mn site influences the double exchange interaction, altering the material's structural properties. The changes in properties are also highly dependent on the doping concentration.

Efforts to engineer materials by doping cite A with Ba and cite B with Fe have been made to investigate perovskite's structural, magnetic, photocatalytic, and electronic properties[9–18]. Fe is an exciting dopant in tandem with Mn because their ion radii are not much different[19], so doping does not significantly alter the crystal structure. Consequently, lattice effects on electrical and magnetic properties can be neglected, and effects due to variations in the electron

configuration of the different ions can be accessed. Fe can be used as a control parameter to vary this manganite's magnetic and transport properties [16]. The obstacle is that the synthesis of $La_{0.7}Ba_{0.3}Mn_{(1-x)}Fe_xO_3$, which is purely single-phase, becomes difficult. Some research that comes close is $La_{0.7-x}Y_xBa_{0.2}Mn_{1-x}Fe_xO_3$ ($x = 0 - 0.3$)[17], $La_{0.8}Ba_{0.2}Mn_{1-x}Fe_xO_3$ ($x = 0 - 0.1$)[18], and $La_{0.7}Ba_{0.3}Mn_{1-x}Fe_xO_3$ ($x = 0, 0.02$)[20], this motivates us to conduct a theoretical study to determine the structural properties of $La_{0.7}Ba_{0.3}Mn_{(1-x)}Fe_xO_3$ at high doping content.

Researchers have undertaken multiple endeavors to forecast the value of perovskite lattice parameters by examining a comprehensive database of perovskite compounds [21-22] and using SPuDS[23]. In this study, we performed simulations on the XRD pattern of lanthanum manganate perovskite material, specifically $La_{0.7}Ba_{0.3}Mn_{(1-x)}Fe_xO_3$, to investigate the effects of doping. The study encompasses five variables with varying constant x values (0, 0.1, 0.2, 0.3, 0.4, and 0.5). Subsequently, we compared the simulation results with experimental findings. The simulations were conducted using first-principle calculations using the Cambridge Serial Total Energy Package (CASTEP) Academic program[24].

METHOD

The basic structure we reference is $LaMnO_3$[25], which has a space group R-3c trigonal with the hexagonal axis. This determination is based on the results of calculations using the Goldsmidtch factor (t_G)[26-27],

$$one t_G = \frac{0.7 r_{La} + 0.3 r_{Ba} + r_O}{\sqrt{2}[(1-x)r_{Mn} + x r_{Fe} + r_O]}, \tag{1}$$

where r is the atomic radius, for r_{La}, r_{Ba}, r_{Mn}, r_{Fe}, and r_O values are 117.2, 149, 72, 69, and 128 pm [19]. The calculation result of Equation (1) for the range of $x = 0 - 0.5$ values is $t_G = 0.891 - 0.898$, which is known to be in the range of rhombohedral or orthorhombic structures reaching stability in the range of $0.89 < t_G < 1.2$ [26-28].

We use CASTEP Academic version 20.11[24]. CASTEP is software implemented with density field theory (DFT) by solving the Khon-Sham equation[29] to perform theoretical simulations of material properties from the first principles. In the calculation initiation process, we use the functional GGA+PBE[30], ultrasoft pseudopotentials[31], and the BFGS algorithm[32]. For the doping technique, we mix the doping atoms at the host atom site by modifying the occupancy or weight according to the doping proportion or mixture atoms; these changes are added in the .cell file as input to the CASTEP file. Note that in performing doping, it is more advisable to expand the unit cell with supercells and replace the atoms directly at certain positions for more realistic calculation results because the periodicity is better preserved than the atom mixture. However, the computation becomes more expensive and longer, so this research uses the atom-atom mixture doping technique. In the .param input file, CASTEP is set to use the Geometry Optimization task for unit cell relaxation with a cut-off energy configuration of 340 eV and k-points of 5x5x2. CASTEP will stop calculating if it reaches the convergent criteria: sixnendsy 5×10^{-6} eV/atom, maximum force 0.01 eV/Å, maximum stress 0.02 Gpa, and maximum displacement 5×10^{-4} Å.

Next, the elastic constant is calculated using CASTEP to determine the mechanical properties of a crystal structure, employing the finite strain theory method [33], where the elasticity constant is calculated by assigning the strain value (ε_j) to calculate the stress (σ_i) which is proportional to the elastic stiffness coefficient (C_{ij}). Furthermore, the values of Bulk Modulus (B), Shear (G), Young (E), Poisson's ratio (v), and Hardness (H) can be calculated using the information from C_{ij} with the formulas of Voigt[34], Reuss[35], dan Hill[36].

RESULTS AND DISCUSSION

The output of the geometry optimization task is information on the relaxed lattice parameters for each doping concentration. We used the Mercury program[37] to simulate the diffraction pattern with a parameter set of step scan 0.001°, λ_{Cu}, and full-weight half maximum 0.3°. Furthermore, we used Vesta[38] to model the 3D unit cell crystal. The Equation (2) used to describe the XRD diffraction pattern simulation is

$$I_{hkl} = \sum_i |F_{hkl}|_i^2 \times p_i \times PL(\theta) \times \beta_i \times M_i + I_{bcg}, \tag{2}$$

with F_{hkl} is the structure factor, p is multiplicity, $PL(\theta)$ is Lorentz polarization, β is full-weight half maximum, M is the temperature factor, and I_{bcg} is background. In this case, we set $I_{bcg} = 0$ (pure crystal without amorphous) and excluded the temperature factor ($M = 1$) to simplify the calculation.
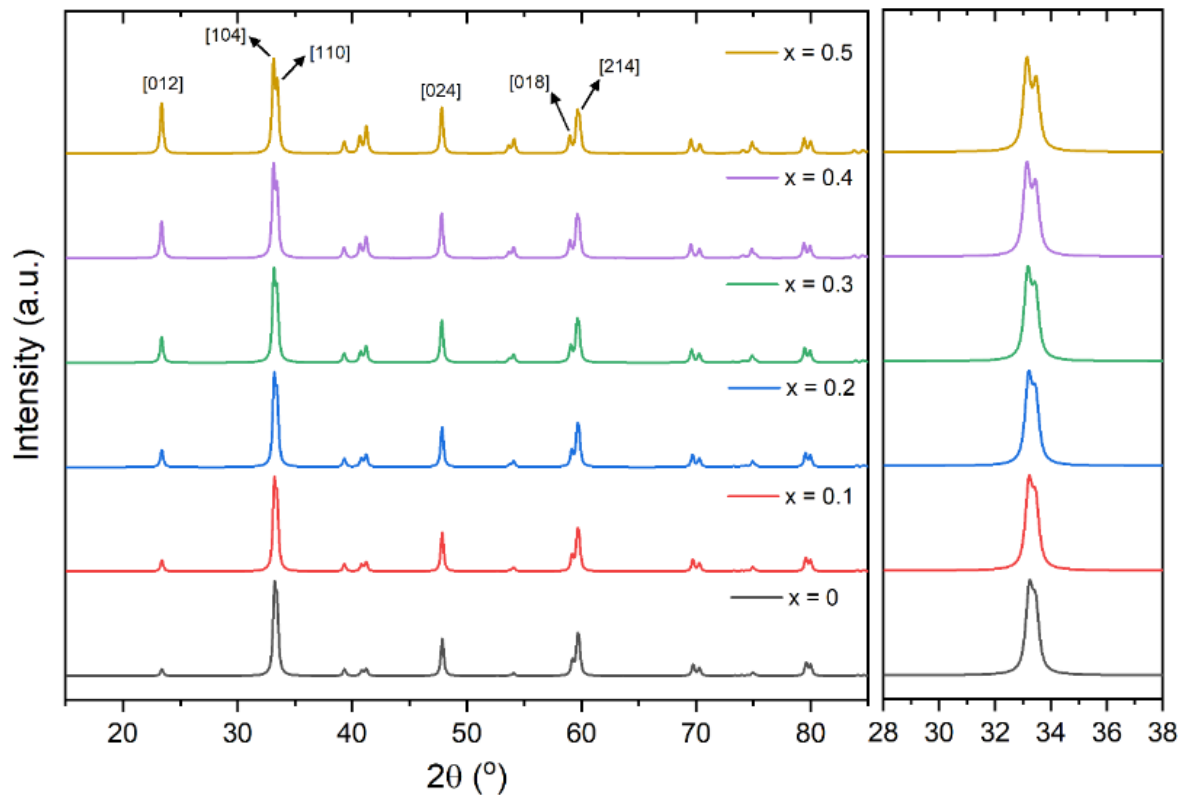

Figure 1. XRD simulation pattern of $La_{0.7}Ba_{0.3}Mn_{(1-x)}Fe_xO_3$ ($x = 0 - 0.5$)

Figure 1 shows the simulated diffraction pattern of $La_{0.7}Ba_{0.3}Mn_{(1-x)}Fe_xO_3$, is a very significant difference can be seen from hkl [012], whose relative intensity of the diffraction pattern gets higher as the value of doping concentration increases; this happens because the slices in hkl [012] are dominantly about O^{-2} ions, as shown in Figure 2(a), and it can be seen in Table 2 and Figure 2(b) that the consequence of doping Fe^{3+} content on Mn^{3+} causes the position of O^{-2} atoms to shift in the low x-coordinate, thus making the O^{-2} content approach and hit the hkl [012] slice. Splitting occurs at high peak positions, namely at hkl [104] and [110]. More details can be seen in Table 1.

Table 1. Positions (2θ) and intensity peaks of $La_{0.7}Ba_{0.3}Mn_{(1-x)}Fe_xO_3$ (x = 0 – 0.5) at six prominent peaks, including experimental data as a comparison.

Simulation Data		hkl					
		[012]	[104]	[110]	[024]	[030]	[214]
$x = 0$	2θ	23.40	33.24	33.41	47.86	59.22	59.69
	Intensity	7.32	100	89.39	39.40	18.73	45.62
$x = 0.1$	2θ	23.40	33.23	33.40	47.85	59.19	59.68
	Intensity	11.84	100	87.93	40.90	18.81	46.13
$x = 0.2$	2θ	23.39	33.21	33.41	47.84	59.16	59.67
	Intensity	18.00	100	86.50	42.26	18.93	46.64
$x = 0.3$	2θ	23.38	33.18	33.42	47.82	59.08	59.64
	Intensity	26.69	100	83.94	44.40	19.02	46.79
$x = 0.4$	2θ	23.37	33.14	33.43	47.80	58.99	59.63
	Intensity	38.43	100	81.26	46.77	19.12	46.49
$x = 0.5$	2θ	23.38	33.14	33.46	47.81	58.98	59.65
	Intensity	53.26	100	79.69	48.48	19.25	46.63
Experimental Data							
$LaMnO_3$ [25]	2θ	22.96	32.53	32.86	46.91	58.04	58.25
	Intensity	31.03	97.98	100	57.42	19.43	34.56
$La_{0.8}Ba_{0.2}MnO_3$ [17]	2θ	22.74	32.33	32.42	46.44	57.67	57.73
	Intensity	28.97	99.69	100	61.59	17.22	33.57

For comparison, we show the experimental results of $LaMnO_3$ and $La_{0.7}Ba_{0.3}MnO_3$. Overall, the difference in peak position (2θ) between the experimental and simulation results is as far as one order of magnitude, and the most significant is in the position of the maximum relative peak, where in the experimental results, the relative maximum peak is at hkl [110] and [104] in the simulation. However, these two positions are prone to maximum peak alternation because the difference in intensity height is not too significant, so any change in content in the unit cell will affect the condition of the two peaks, in this case, O^{-2}. Overall, the doping concentration significantly influences. This discrepancy directly affects the value of the structure factor, which, in turn, impacts the intensity height. In contrast to the peak position (2θ), the alterations in the unit cell lattice parameters have a more pronounced association with the observed peak height.

Table 2 shows that the value of lattice parameters has increased not so significantly, which is only on the order of magnitude 10^{-3} for the a-direction and c-direction as the doping value of Fe increases. Similar results are shown in the experimental results of Ghodhbane et al.[18] on Fe doping x = 0.1, which only increased by 0.001 in the a-direction and 0.004 for the c-direction when compared to the experimental results of Kallel[17] et al. Moreover, Baazoui et al.[16] reported that the volume of the cell in $La_{0.67}Ba_{0.33}Mn_{1-x}Fe_xO_3$ (x = 0, 0.15) samples exhibits a minor fluctuation, ranging from 358.86(3) to 359.71(2) $Å^3$, as the iron content increases, which iron is incorporated into the samples in the form of Fe^{3+}. Given that Mn^{3+} and Fe^{3+} possess nearly identical ionic radii, the structural impact of Fe doping is not significant and, thus, hard to detect.
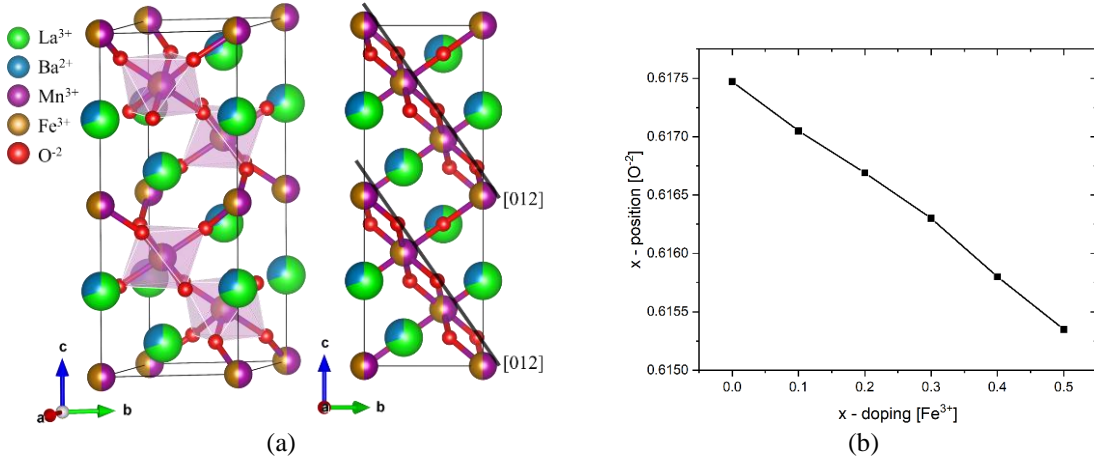
Figure 2. (a) 3D models of the crystal structure of $La_{0.7}Ba_{0.3}Mn_xFe_{(1-x)}O_3$, (b) atomic position of O^{-2} ions in a unit cell at the x-axis.

Significant differences occur at the B-O-B angle, which impacts the bandwidth (W)[26].

$$W = \frac{\cos\left[\frac{1}{2}(\pi - \phi_{B-O-B})\right]}{d_{B-O}^{3.5}}, \quad (3)$$

with ϕ_{B-O-B} is the angle formed from site B atoms, in this case, Mn and Fe towards O, d_{B-O} is the distance between atoms in sites B and O. It can be seen in Table 2 that the high doping content does not affect the inter-atomic distance.

Table 2. The lattice parameter of $La_{0.7}Ba_{0.3}Mn_{(1-x)}Fe_xO_3$ (x = 0 – 0.5) included experimental data as a comparison.

x	a (Å)	c (Å)	V (Å^3)	ρ (g/cm^3)	d_{B-O} (Å)	ϕ_{B-O-B} (°)	W (10^{-2})
0	5.3532	13.246	328.727	11.492	2.001	143.357	3.002
0.1	5.3533	13.254	328.937	13.176	2.000	143.486	2.998
0.2	5.3534	13.260	329.105	13.170	1.999	143.596	2.995
0.3	5.3541	13.278	329.622	13.149	2.000	143.724	2.981
0.4	5.3530	13.297	329.971	13.135	1.999	143.888	2.974
0.5	5.3498	13.300	329.662	13.147	1.999	144.030	2.964
Experiment data							
$La_{0.7}Ba_{0.3}MnO_3$ [17]	5.551	13.479	359.72	12.025	1.973	165.103	9.262
$La_{0.7}Ba_{0.3}Mn_{0.9}Fe_{0.1}O_3$ [18]	5.554	13.483	360.20	12.014	1.974	165.101	9.251

Although the experimental and simulated bandwidth values are very different, both have the same trend, namely, the value of W decreases with the high doping content at the Mn site. Bandwidth physically explains the double exchange in the perovskite unit cell. Although, Fe^{3+} ions do not participate in the double exchange interaction phenomenon towards Mn^{3+}[39]. Thus, in line with Troyanchuk et al. reports that the ferromagnetic double exchange interaction weakens and strengthens the super-exchange interaction that supports the antiferromagnetic coupling between Mn^{4+}–O–Mn^{4+}, Mn^{4+}–O–Fe^{3+}, and Fe^{3+}–O–Fe^{3+} [40]. The reduction of the double exchange interaction can be seen from the decrease in the bandwidth value [41].

Table 3. Elastic stiffness Coefficien of $La_{0.7}Ba_{0.3}Mn_{(1-x)}Fe_xO_3$ ($x = 0 - 0.5$).

x	C_{ij} (GPa)					
	C_{11}	C_{33}	C_{44}	C_{12}	C_{13}	C_{14}
0	313.343	201.921	59.913	185.338	142.427	-1.177
0.1	309.763	217.745	55.772	182.495	134.394	0.494
0.2	301.296	204.243	53.048	174.642	132.065	1.460
0.3	268.026	182.560	49.602	141.656	103.699	2.730
0.4	259.364	182.572	54.281	138.071	99.493	3.168
0.5	256.842	174.894	54.151	141.189	93.755	3.221

The elastic constant is a significant parameter to determine the mechanical property of a material through the elastic stiffness coefficient, C_{ij}. In this case, the C_{ij} values for $La_{0.7}Ba_{0.3}Mn_{(1-x)}Fe_xO_3$ ($x = 0 - 0.5$) crystal structure are summarized in Table 3. The rhombohedral crystal system has eight values of C_{ij}, C_{11}, C_{33}, C_{44}, C_{12}, C_{13}, C_{14}, C_{15} and C_{66} [42]. The rhombohedral structure has only six C_{ij} values since $C_{14} = C_{15}$ and $C_{66} = (C_{11} - C_{12})/2$. The simulated structure is in a stable state as it fulfills the stable condition for rhombohedral structures[42]:

$$C_{11} > |C_{12}|; C_{44} > 0$$
$$C_{13}^2 < C_{33}(C_{11} + C_{12})/2 \qquad \qquad . \qquad (4)$$
$$C_{14}^2 + C_{15}^2 < C_{44}(C_{11} - C_{12})/2 = C_{44}C_{66}$$

The Fe^{3+} doping content greatly affects the value of C_{ij}. The higher value of x decreases the elastic stiffness coefficient of C_{11}, C_{33}, C_{44}, C_{12}, and C_{13}. Nevertheless, the opposite is true for C_{14}. Our results align with those of Koriba et al. [43]; the values of C_{11} and C_{33} are significantly larger than the other elastic stiffness coefficients, resulting in elastic anisotropy of the structure. C_{11} is greater than C_{33}, indicating that the compressibility along the a and b axes is greater than the c axis. Hence, the coupling along the a and b axes is powerful for rhombohedral $LaMnO_3$. As a result, Fe doping has little effect on the lattice parameter a, as shown in Table 2.

Some mechanical properties that can be calculated from the elastic stiffness coefficient are Bulk (B), Shear (G), and Young (E) moduli, as well as Poisson's ratio (ν) and hardness (H). The calculation of these properties uses the Voigt and Reuss approach, namely for Bulk and Shear modulus.[34-35]:

$$B_V = \frac{1}{9}[2(C_{11} + C_{12} + 2C_{13}) + C_{33}], \qquad (5)$$

$$G_V = \frac{1}{30}[C_{11} + C_{12} + 2(C_{33} - 2C_{13}) + 12(C_{44} + C_{66})], \qquad (6)$$

$$B_R = \frac{(C_{11}+C_{12})C_{33}-2C_{13}^2}{C_{11}+C_{12}+2C_{33}-4C_{13}}, \qquad (7)$$

$$G_R = \frac{5}{2}\frac{[(C_{11}+C_{12})C_{33}-2C_{13}^2]C_{44}C_{66}}{3B_VC_{44}C_{66}+[(C_{11}+C_{12})C_{33}-2C_{13}^2](C_{44}+C_{66})}, \qquad (8)$$

for Hill approximation [36] can be calculated as the average value between Voigt and Reuss:

$$B_H = \frac{1}{2}(B_V + B_R), \quad G_H = \frac{1}{2}(G_V + G_R). \qquad (9)$$

Bulk and Shear modulus can be used to calculate Young's modulus and Poisson's ratio[44] :

$$E = \frac{9BG}{3B+G}, \quad v = \frac{3B-2G}{2(3B+G)}, \tag{10}$$

Vickers hardness is calculated based on Tian[45] with the following formula

$$H_v = 0.92 \left(\frac{G}{B}\right)^{1.137} G^{0.708}. \tag{11}$$

The results of the mechanical property calculations are summarized in Table 4. The Bulk, Shear, and Young's modulus values decrease as the Fe doping content increases. While for Poisson's ratio, there is no significant difference. On the other hand, Hardeness experienced a significant increase, as we know that material with an enormous Bulk modulus value has a powerful bond between atoms on average. A large shear modulus indicates that the material has a high resistance to reversible deformation, and the higher the Young modulus value, the stiffer the material. So doping Fe content makes the $La_{0.7}Ba_{0.3}MnO_3$ Perovskite material weaken its atomic bonds, the range of deformation occurs, and the more flexible. According to Ikhsan et al., increasing the concentration of iron (Fe) doping in Lanthanum perovskite induces structural deformation. Furthermore, doping can also modulate the material's flexibility, owing to its capability to modify the electronic structure, thereby influencing its mechanical properties[46].

Table 4. Mechanical properties of $La_{0.7}Ba_{0.3}Mn_{(1-x)}Fe_xO_3$ (x = 0 – 0.5) were calculated using the Voigt (V), Reuss (R), and Hill (H) approach.

Mechanical properties		\(x\)					
		0	0.1	0.2	0.3	0.4	0.5
Bulk	V	196.55	193.32	187.15	157.41	152.82	149.55
Modulus	R	180.65	182.13	174.99	148.01	144.71	139.57
(B)	H	188.60	187.72	181.07	152.71	148.77	144.56
Shear	V	60.66	60.77	58.42	57.12	58.12	57.22
Modulus	R	59.33	59.80	57.24	55.64	57.20	56.18
(G)	H	60.00	60.28	57.83	56.38	57.66	56.70
Young	V	165.00	165.01	158.75	152.86	154.75	111.41
Modulus	R	160.44	161.70	154.85	148.32	151.62	102.12
(E)	H	162.73	163.36	156.81	150.60	153.19	106.77
Poisson	V	0.36	0.36	0.36	0.34	0.33	0.33
Rasio	R	0.35	0.35	0.35	0.33	0.33	0.32
(\(v\))	H	0.36	0.35	0.36	0.34	0.33	0.33
	V	3.24	3.18	3.20	2.76	2.63	2.61
\(B/G\)	R	3.04	3.05	3.06	2.66	2.53	2.48
	H	3.14	3.11	3.13	2.71	2.58	2.55
Hardness (Hv)	V	4.42	4.52	4.36	5.09	5.44	5.42
	R	4.67	4.70	4.53	5.20	5.62	5.66
	H	4.54	4.61	4.44	5.15	5.53	5.54

Poisson's ratio shows that the value of $v < 0.15$ is owned by materials with strong covalent bonds, at $0.16 \leq v \leq 0.3$ is a material with ionic-covalent bonds, and for $v > 0.33$ is characteristic of metallic materials[47]. In this research, the Poisson's ratio value range of $0.36 \lesssim v \lesssim 0.33$ is obtained, indicating that doping Fe content up to 0.5 of $La_{0.7}Ba_{0.3}Mn_{(1-x)}Fe_xO_3$ material has metallic bonds and is heading towards the ionic-covalent bond. This result is quite

confusing because we knew that typical perovskite has an ionic-covalent bond. However, according to Huang et al., single crystal perovskite may have an unusual Poisson's ratio depending on its crystal structure, for rhombohedral structure has a range of Poisson's ratio $-0.421 \leq \nu \leq 0.883$[48]. Ergo, it is not accurate to say that Poisson's ratio can be used to directly determine the type of bonding (covalent, ionic, metallic) in a material; for example, both a metal with metallic bonding and a polymer with covalent bonding can have similar Poisson's ratios, even though their types of bonding are different. Poisson's ratio is influenced by many factors, including the material's crystal structure, defect structure, and temperature[48–50]. Further examination and addition of CASTEP parameters are needed for more accurate calculation. The B/G ratio provides information on how brittle and ductile material is, with the rule of the value range at 1.75 as a reference point, known as Pugh's criterion, where fragile < 1.75 < ductile[51]. In this case, the material still has a ductile character. However, the increasing value of x content makes the $La_{0.7}Ba_{0.3}MnO_3$ reduce their ductility.

The output of the elastic constant task also includes some interesting information, such as the universal anisotropic index (A^U)[52], Speed of Sound (v_m), and Elastic Debye Temperature (θ_D)[53], which can be calculated using the following Equation

$$A^U = 5\frac{G_V}{G_R} + \frac{B_V}{B_R} - 6, \tag{12}$$

$$v_m = \left\{ \frac{1}{3}\left[\frac{2}{(G_H/\rho)^{3/2}} + \frac{1}{((B_H+4G_H/3)/\rho)^{3/2}} \right]\right\}^{-\frac{1}{3}}, \tag{13}$$

$$\theta_D = \frac{h}{k}\left[\frac{3q}{4\pi}\frac{N_A\rho}{M}\right]^{1/3} v_m, \tag{14}$$

with h as Planck constant, k as Boltzmann constant, N_A is the Avogadro number, q is the number of atoms in unit cells, M is molecule mass in the unit cell, ρ is density. The results of the calculation of Equations (12) - (14) are summarized in Table 5.

Table 5. Speed of sound (v_m), universal anisotropic index (A^U), and Debye Temperature for $La_{0.7}Ba_{0.3}Mn_{(1-x)}Fe_xO_3$ (x = 0 – 0.5).

x	v_m (m/s)	A^U	θ_D (K)
0	3213.00	0.20	430.25
0.1	3224.12	0.14	431.65
0.2	3155.31	0.17	422.37
0.3	3107.14	0.20	415.70
0.4	3146.19	0.14	420.78
0.5	3116.78	0.16	416.97

If $A^U = 0$ indicates isotropic material. The higher than 0, the more anisotropic the material is, so for $La_{0.7}Ba_{0.3}Mn_{(1-x)}Fe_xO_3$ material is anisotropic, meaning that the representation of mechanical properties is different in various directions. The last property that is no less important is Debye temperature, which can be calculated from the speed of sound in the material, where the higher the value of θ_D, the higher the thermal conductivity. It is known that there is a decrease in thermal conductivity when doping Fe content increases.

CONCLUSION

We have conducted a theoretical investigation of $La_{0.7}Ba_{0.3}MnO_3$ material with Fe^{3+} doping at Mn^{3+} sites at $x = 0 - 0.5$ using the CASTEP Academic program to display the material's structural properties regarding diffraction patterns and mechanical properties. Fe^{3+} content doping affects the peak height of the diffraction pattern more than the shift in peak position, with some peaks increasing in height due to Fe^{3+} having a relatively higher atomic form factor than Mn. However, Fe^{3+} doping decreases $Mn^{3+} - O^{-2} - Mn^{3+}$ double exchange interaction characterized by decreased bandwidth (W) value. From the mechanical properties point of view, it is shown that Fe doping to Mn sites is responsible for the reduction of Bulk, Shear, and Young's modulus values of $La_{0.7}Ba_{0.3}Mn_{(1-x)}Fe_xO_3$ perovskite. Furthermore, it is known that $La_{0.7}Ba_{0.3}Mn_{(1-x)}Fe_xO_3$ is anisotropic, and the Debye temperature as an indicator of thermal conductivity also decreases as Fe^{3+} doping increases.

REFERENCES

1   Xia, W., Pei, Z., Leng, K., & Zhu, X. 2020. Research Progress in Rare Earth-Doped Perovskite Manganite Oxide Nanostructures. *Nanoscale Research Letters*, *15*(1), 9.

2   Zeng, Z., Xu, Y., Zhang, Z., Gao, Z., Luo, M., Yin, Z., Zhang, C., Xu, J., Huang, B., Luo, F., Du, Y., & Yan, C. 2020. Rare-earth-containing perovskite nanomaterials: design, synthesis, properties and applications. *Chemical Society Reviews*, *49*(4), 1109–1143.

3   Wang, H., Zhang, H., Su, K., Huang, S., Tan, W., & Huo, D. 2020. Structure, charge ordering, and magnetic properties of perovskite $Sm_{0.5}Ca_{0.5}MnO_3$ manganite. *Journal of Materials Science: Materials in Electronics*, *31*(17), 14421–14425.

4   Li, B., Tian, F., Cui, X., Xiang, B., Zhao, H., Zhang, H., Wang, D., Li, J., Wang, X., Fang, X., Qiu, M., & Wang, D. 2022. Review for Rare-Earth-Modified Perovskite Materials and Optoelectronic Applications. *Nanomaterials*, *12*(10), 1773.

5   Badelin, A. G., Karpasyuk, V. K., Merkulov, D. I., Eremina, R. M., Yatsyk, I. V., Shestakov, A. V., & Estemirova, S. Kh. 2020. Effect of Iron Doping on Structural, Magnetic, and Electrical Characteristics of Manganites in $La_{0.7}Sr_{0.3}Mn_{0.9}Zn_{0.1-x}Fe_xO_3$ ($0 \leq x \leq 0.1$) System. *Inorganic Materials: Applied Research*, *11*(2), 435–440.

6   Jayakumar, G., Poomagal, D. S., Albert Irudayaraj, A., Dhayal Raj, A., Kethrin Thresa, S., & Akshadha, P. 2020. Study on structural, magnetic and electrical properties of perovskite lanthanum strontium manganite nanoparticles. *Journal of Materials Science: Materials in Electronics*, *31*(23), 20945–20953.

7   Hassayoun, O., Baazaoui, M., Laouyenne, M. R., Hosni, F., Hlil, E. K., Oumezzine, M., & Farah, Kh. 2019. Magnetocaloric effect and electron paramagnetic resonance studies of the transition from ferromagnetic to paramagnetic in $La_{0.8}Na_{0.2}Mn_{1-x}NixO_3$ ($0 \leq x \leq 0.06$). *Journal of Physics and Chemistry of Solids*, *135*, 109058.

8   Oumezzine, Ma., Sales, H. B., Selmi, A., & Hlil, E. K. 2019. Pr^{3+} doping at the A-site of $La_{0.67}Ba_{0.33}MnO_3$ nanocrystalline material: assessment of the relationship between structural and physical properties and Bean–Rodbell model simulation of disorder effects. *RSC Advances*, *9*(44), 25627–25637.

9   Baazaoui, M., Boudard, M., & Zemni, S. 2011. Magnetocaloric properties in $Ln_{0.67}Ba_{0.33}Mn_{1-x}Fe_xO_3$ (Ln=La or Pr) manganites. *Materials Letters*, *65*(14), 2093–2095.

10 M. G., S., Kumar H. L., S., & Shwetha. 2023. Morphological, structural, electrical impedance, and equivalent circuit analysis of polypyrrole/barium substituted lanthanum manganite ($La_{0.7}Ba_{0.3}MnO_3$) perovskite nanocomposites. *International Journal of Polymer Analysis and Characterization*, *28*(3), 241–255.

11 Koner, S., Deshmukh, P., Ahlawat, A., Karnal, A. K., & Satapathy, S. 2021. Studies on structural, dielectric, impedance spectroscopy and magneto-dielectric properties of $La_{0.7}Ba_{0.3}MnO_3$/P (VDF-TrFE) multiferroic (0–3) nanocomposite films. *Journal of Alloys and Compounds*, *868*, 159104.

12 Koner, S., Deshmukh, P., Ali Khan, A., Ahlawat, A., Karnal, A. K., & Satapathy, S. 2020. Multiferroic properties of $La_{0.7}Ba_{0.3}MnO_3$/P(VDF-TrFE) (0-3) nanocomposite films. *Materials Letters*, *261*, 127161.

13 Esmaeili, S., Ehsani, M. H., & Fazli, M. 2020. Structural, optical and photocatalytic properties of $La_{0.7}Ba_{0.3}MnO_3$ nanoparticles prepared by microwave method. *Chemical Physics*, *529*, 110576.

14 Sazali, M. S., Ibrahim, N., Mohamed, Z., Rajmi, R., & Yahya, A. K. 2021. Effect of Fe^{3+} Partial Substitution at Mn-Site on Electroresistance Behaviour in $La_{0.7}Ba_{0.3}Mn_{1-x}Fe_xO_3$(x = 0 and 0.02) Manganites. *Solid State Phenomena*, *317*, 3–9.

15 Esmaeili, S., Ehsani, M. H., & Fazli, M. 2020. Photocatalytic activities of $La_{0.7}Ba_{0.3}MnO_3$ nanoparticles. *Optik*, *216*, 164812.

16 Baazaoui, M., Zemni, S., Boudard, M., Rahmouni, H., Gasmi, A., Selmi, A., & Oumezzine, M. 2009. Magnetic and electrical behavior of $La_{0.67}Ba_{0.33}Mn_{1-x}Fe_xO_3$ perovskites. *Materials Letters*, *63*(24–25), 2167–2170.

17 Kallel, N., Abdelkhalek, S. Ben, Kallel, S., Peña, O., & Oumezzine, M. 2010. Structural and magnetic properties of $(La_{0.70-x}Y_x)Ba_{0.30}Mn_{1-x}Fe_xO_3$ perovskites simultaneously doped on A and B sites (0.0≤x≤0.30). *Journal of Alloys and Compounds*, *501*(1), 30–36.

18 Ghodhbane, S., Dhahri, A., Dhahri, N., Hlil, E. K., & Dhahri, J. 2013. Structural, magnetic and magnetocaloric properties of La0.8Ba0.2Mn1−xFexO3 compounds with 0⩽x⩽0.1. *Journal of Alloys and Compounds*, *550*, 358–364.

19 Shannon, R. D. 1976. Revised effective ionic radii and systematic studies of interatomic distances in halides and chalcogenides. *Acta Crystallographica Section A*, *32*(5), 751–767.

20 Sazali, M. S., Ibrahim, N., Mohamed, Z., Rajmi, R., & Yahya, A. K. 2021. Effect of Fe3+ Partial Substitution at Mn-Site on Electroresistance Behaviour in $La_{0.7}Ba_{0.3}Mn_{(1-x)}Fe_{(x)}O3$(x = 0 and 0.02) Manganites. *Solid State Phenomena*, *317*, 3–9.

21 Ubic, R., Tolman, K., Talley, K., Joshi, B., Schmidt, J., Faulkner, E., Owens, J., Papac, M., Garland, A., Rumrill, C., Chan, K., Lundy, N., & Kungl, H. 2015. Lattice-constant prediction and effect of vacancies in aliovalently doped perovskites. *Journal of Alloys and Compounds*, *644*, 982–995.

22 Smith, E., Wander, O., & Ubic, R. 2020. Empirical models of trigonal distortions and polarization in perovskites. *Journal of the American Ceramic Society*, *103*(12), 7172–7187.

23 Lufaso, M. W., & Woodward, P. M. 2001. Prediction of the crystal structures of perovskites using the software program *SPuDS*. *Acta Crystallographica Section B Structural Science*, *57*(6), 725–738.

24 Clark, S. J., Segall, M. D., Pickard, C. J., Hasnip, P. J., Probert, M. I. J., Refson, K., & Payne, M. C. 2005. First principles methods using CASTEP. *Zeitschrift Für Kristallographie - Crystalline Materials*, *220*(5–6), 567–570.

25 Huang, T.-S., Chen, C.-H., & Tai, M.-F. 2001. Studies on Crystal Structure and Magnetic Scaling Behavior of Perovskite-Like $(La_{1-x} Pb_x)MnO_3$ System with $x = 0$ - 0.5. *MRS Proceedings*, *674*, U3.4.

26 Zahrin, A., Azhar, N. A., Ibrahim, N., & Mohamed, Z. 2022. Structural, Magnetic, and Electrical Properties and Magnetoresistance of Monovalent K-Substituted $La_{0.7}Ba_{0.3-x}K_xMnO_3$ ($x = 0$ and 0.04) Manganite. *Condensed Matter*, *7*(3), 51.

27 Jeddi, M., Massoudi, J., Gharsallah, H., Ahmed, S. I., Dhahri, E., & Hlil, E. K. 2021. Impact of potassium substitution on structural, magnetic, magnetocaloric and magneto-transport properties of $Nd_{0.6}Sr_{0.4-x}K_xMnO_3$ ($0.0 \leq x \leq 0.2$) manganite. *Journal of Materials Science: Materials in Electronics*, *32*(14), 18751–18764.

28 Messaoui, I., Riahi, K., Kumaresavanji, M., Cheikhrouhou Koubaa, W., & Cheikhrouhou, A. (2018). Potassium doping induced changes of magnetic and magnetocaloric properties of $La_{0.78}Cd_{0.22-x}K_xMnO_3$ ($x = 0.00$, 0.10, 0.15 and 0.20) manganites. *Journal of Magnetism and Magnetic Materials*, *446*, 108–117.

29 Kohn, W., & Sham, L. J. 1965. Self-Consistent Equations Including Exchange and Correlation Effects. *Physical Review*, *140*(4A), A1133–A1138.

30 Perdew, J. P., Burke, K., & Ernzerhof, M. 1996. Generalized Gradient Approximation Made Simple. *Physical Review Letters*, *77*(18), 3865–3868.

31 Francis, G. P., & Payne, M. C. 1990. Finite basis set corrections to total energy pseudopotential calculations. *Journal of Physics: Condensed Matter*, *2*(19), 4395–4404.

32 Pfrommer, B. G., Côté, M., Louie, S. G., & Cohen, M. L. 1997. Relaxation of Crystals with the Quasi-Newton Method. *Journal of Computational Physics*, *131*(1), 233–240.

33 Truesdell, C. 1984. Murnaghan's Finite Deformation of an Elastic Solid (1952). In *An Idiot's Fugitive Essays on Science* (pp. 148–150). Springer New York.

34 Voigt, W. 1928. Lehrbuch der kristallphysik. *Teubner, Leipzig/Berlin*, *34*.

35 Reuss, A. 1929. Berechnung der Fließgrenze von Mischkristallen auf Grund der Plastizitätsbedingung für Einkristalle. *ZAMM - Zeitschrift Für Angewandte Mathematik Und Mechanik*, *9*(1), 49–58.

36 Hill, R. 1952. The Elastic Behaviour of a Crystalline Aggregate. *Proceedings of the Physical Society. Section A*, *65*(5), 349–354.

37 Macrae, C. F., Sovago, I., Cottrell, S. J., Galek, P. T. A., McCabe, P., Pidcock, E., Platings, M., Shields, G. P., Stevens, J. S., Towler, M., & Wood, P. A. 2020. Mercury 4.0: from visualization to analysis, design and prediction. *Journal of Applied Crystallography*, *53*(1), 226–235.

38 Momma, K., & Izumi, F. 2011. VESTA 3 for three-dimensional visualization of crystal, volumetric and morphology data. *Journal of Applied Crystallography*, *44*(6), 1272–1276.

39 Ahn, K. H., Wu, X. W., Liu, K., & Chien, C. L. 1996. Magnetic properties and colossal magnetoresistance of $La(Ca)MnO_3$ materials doped with Fe. *Physical Review B*, *54*(21), 15299–15302.

40 Troyanchuk, I. O., Bushinsky, M. V., Karpinsky, D. V., Tereshko, N. V., Dobryansky, V. M., Többens, D. M., Sikolenko, V., & Efimov, V. 2015. Magnetic interactions in $La_{0.7}Sr_{0.3}Mn_{1-Me}O_3$ (Me=Ga, Fe, Cr) manganites. *Journal of Magnetism and Magnetic Materials*, *394*, 212–216.

41 Ghodhbane, S., Dhahri, A., Dhahri, N., Hlil, E. K., & Dhahri, J. 2013. Structural, magnetic and magnetocaloric properties of La0.8Ba0.2Mn1−xFexO3 compounds with 0⩽x⩽0.1. *Journal of Alloys and Compounds*, *550*, 358–364.

42 Mouhat, F., & Coudert, F.-X. 2014. Necessary and sufficient elastic stability conditions in various crystal systems. *Physical Review B*, *90*(22), 224104.

43 Koriba, I., Lagoun, B., Guibadj, A., Belhadj, S., Ameur, A., & Cheriet, A. 2021. Structural, electronic, magnetic and mechanical properties of three LaMnO3 phases: Theoretical investigations. *Computational Condensed Matter*, *29*, e00592.

44 Coulson, C. A. 1958. Physical Properties of Crystals. By J. F. Nye . Pp. xv, 322, 50s. 1957. (Oxford: Clarendon Press). *The Mathematical Gazette*, *42*(342), 329–330.

45 Tian, Y., Xu, B., & Zhao, Z. 2012. Microscopic theory of hardness and design of novel superhard crystals. *International Journal of Refractory Metals and Hard Materials*, *33*, 93–106.

46 Ikhsan, F., Kurniawan, B., Razaq, D. S., Munazat, D. R., & Putri, Witha. B. K. 2023. *Effect of Fe and Ti doping on Mn site of $La_{0.7}Ba_{0.3}Mn_{0.85}Fe_{0.15-x}Ti_xO_3$ as electromagnetic wave absorbing material*. 060004.

47 Antonio, J. E., Cervantes, J. M., Rosas-Huerta, J. L., Romero, M., Escamilla, R., & Carvajal, E. 2021. Exposed Surface and Confinement Effects on the Electronic, Magnetic, and Mechanical Properties of $LaTiO_3$ Slabs. *IEEE Transactions on Magnetics*, *57*(6), 1–4.

48 Huang, C. W., Ren, W., Nguyen, V. C., Chen, Z., Wang, J., Sritharan, T., & Chen, L. 2012. Abnormal Poisson's ratio and Linear Compressibility in Perovskite Materials. *Advanced Materials*, *24*(30), 4170–4174.

49 Kiely, E., Zwane, R., Fox, R., Reilly, A. M., & Guerin, S. 2021. Density functional theory predictions of the mechanical properties of crystalline materials. *CrystEngComm*, *23*(34), 5697–5710.

50 Carneiro, V., & Puga, H. 2018) Temperature Variability of Poisson's Ratio and Its Influence on the Complex Modulus Determined by Dynamic Mechanical Analysis. *Technologies*, *6*(3), 81.

51 Güler, E., Uğur, Ş., Güler, M., & Uğur, G. 2021. First principles study of structural, elastic, mechanical and electronic properties of nitrogen-doped cubic diamond. *Bulletin of Materials Science*, *44*(1), 1.

52 Ranganathan, S. I., & Ostoja-Starzewski, M. 2008. Universal Elastic Anisotropy Index. *Physical Review Letters*, *101*(5), 055504.

53 Anderson, O. L. 1963. A simplified method for calculating the debye temperature from elastic constants. *Journal of Physics and Chemistry of Solids*, *24*(7), 909–917.